Experimental and numerical analyses of sloshing flows

Yonghwan Kim

Abstract Recently the demand for sloshing analyses is rising because of the construction of large LNG carriers and LNG platforms. This study considers the experimental and numerical observations of strongly nonlinear sloshing flows in ship cargo and their coupling effects with ship motion. Violent sloshing flows in experiments are observed, and two different numerical methods, the finite-difference method and smoothed-particle-hydrodynamics (SPH) method, are applied for the simulation of violent sloshing flows. Several physical issues are introduced in the analysis of sloshing flows, and the corresponding numerical models are described. This study demonstrates that physics-based numerical schemes are essential in the prediction of violent sloshing flows and sloshing-induced impact pressure. To study the sloshing effects on ship-motion, a ship-motion program based on an impulsive response function (IRF) is coupled with the developed numerical models for sloshing analysis. The results show that the nonlinearity of sloshing-induced forces and moments plays a critical role in the coupling effects.

Keywords Coupled analysis · Impulse response function · Ship motion · Sloshing · Smoothed-particle-hydrodynamics (SPH) method

1 Introduction

There are two primary concerns related to sloshing flows in ship hydrodynamics: the prediction of sloshing-induced impact loads on ship structures, and the dynamics of ship motion coupled with sloshing-induced excitation. The former is an important task in the design of internal cargo structures. In particular, this is an essential element in the design of membrane-type liquefied natural gas (LNG) carriers or LNG platforms. The latter has been of interest for the prediction of the dynamic behavior of ship motion. Examples are the anti-rolling tank and capsizing due to green-water sloshing.

Many studies on the ship sloshing problem were carried out in the 1970s and early 1980s for the design of LNG carriers. Recently, the demand for sloshing analyses is rising again for the design of larger LNG carriers and LNG floating-production-storage-offloading (FPSO) vessels. Many numerical studies on sloshing flows have been reported during last two decades. Some representative works have been introduced by

Y. Kim (✉)
Department of Naval Architecture & Ocean Engineering, Seoul National University, Seoul, South Korea
e-mail: yhwankim@snu.ac.kr

Faltinsen [1,2], Bridges [3], Mikelis [4] Wu et al. [5] and Kim [6]. Despite numerous studies, few methods are applicable for actual engineering use such as the simulation of violent flows and the prediction of impact loads.

This study aims to clarify the physical phenomena involved in violent sloshing flows, and the development of proper numerical models for practical use. To this end, both experimental observations and numerical computations are carried out. The results of two experiments for Daewoo and Seoul National University (SNU) are used for observing the physical issues inherent in violent sloshing flows. Based on the experimental observation, technical issues are considered for the accurate prediction of sloshing flows, especially impact loads. The suggested technical issues are reflected by the present numerical methods.

In this study, two numerical methods, a finite-difference method (FDM) and a smoothed-particle-hydrodynamics (SPH) method, are considered. The present two methods have distinct differences in the simulation of sloshing flows: the simulation of global fluid motion using FDM and the simulation of more local flows using SPH. Therefore, a comparison of the computational results by the two methods may provide information for the selection of adequate numerical schemes for sloshing analyses. The finite-difference method applied in the present computation is based on the numerical method introduced by Kim [6]. This method concentrates on the global motion of sloshing flows, adopting the concept of buffer zone. This method has been extended to more complicated geometries [7], e.g. three-dimensional prismatic tanks. This study puts more weight on the application of the SPH method. After the pioneering work of Monaghan [8] for the water-wave problem, the SPH method has been applied to various free-surface problems, especially for strongly nonlinear wave problems. Some representative extensions or applications of the SPH method can be found in the works of Colagrossi and Landrini [9], Iglesias et al. [10], and Oger et al. [11]. The computational results are validated by comparing these with the results of the finite-difference method and/or experimental data.

This study is extended to the analysis of sloshing problems coupled with ship motion. There are some existing studies on the coupling analysis, e.g. [12–15]. According to existing studies, the assumption of linear ship motion seems adequate in the coupled analysis. However, the linear assumption is not valid in sloshing flows. When a nonlinear sloshing flow is considered, the ship motion should be observed in the time domain. To this end, the present study adopts an impulse-response function (IRF). If a set of frequency-domain solutions is available, the IRF can be obtained from the inverse Fourier transform of the frequency-domain solution [16]. For numerical tests, the roll motion of the modified S175 hull equipped with an anti-rolling tank is observed for different wave amplitudes. From this study, it is found that that the nonlinearity of sloshing flow plays a critical role in the coupled problem.
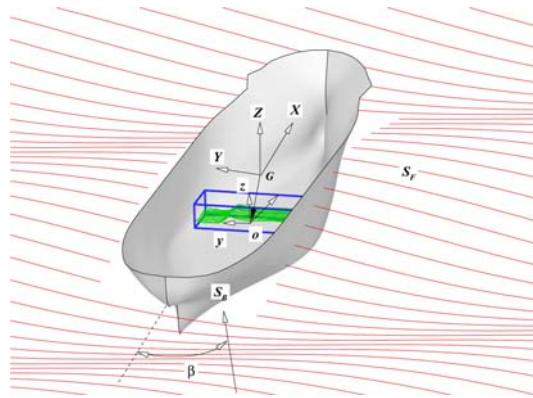
2 Physical problem

2.1 Problem definition

Let us consider a freely floating ship with partially filled tank(s) in incident waves. Two Cartesian coordinate systems can be defined as shown in Fig. 1. A body-fixed coordinate system is adopted on the ship with an origin at the motion center (G), and a local tank-fixed coordinate system is defined for sloshing flows with an origin at the center of tank bottom (o). Internal sloshing flow in the tank is excited by the ship's motion, but the motion of the ship is also affected by the sloshing-induced excitation as well as external wave-induced excitation. Therefore, two problems should be solved simultaneously.

The ship motion can be obtained by solving the equation of motion such that

$$\sum_{j=1}^{6} \left[m_{ij}\ddot{\xi}_j(t) + b_{ij}\dot{\xi}_j(t) + c_{ij}\xi_j(t) \right] = F_i^{\text{external}}(t) + F_i^{\text{internal}}(t), \tag{1}$$

Fig. 1 Coordinate
systems

where $\vec{\xi} = [\xi_j]$ is the displacement of the ship during its motion. m_{ij}, b_{ij} and c_{ij} represent the matrices of mass, damping and restoring coefficients. The force vector $F_j^{\text{exteranl}}(t)$ indicates all the external forces and moments on the ship. The external force includes the diffraction and radiation force. $F_j^{\text{internal}}(t)$ implies the internal force vector due to sloshing. Therefore, to solve Eq. 1, we need to solve all the diffraction, radiation, and sloshing problems.

The ship motion is the primary source of sloshing flow in the tank. The external force acting on a fluid volume due to the ship motion consists of the gravitational force, translational and rotational inertia forces, and takes the following form:

$$\vec{f} = \vec{g} - \frac{\mathrm{d}\vec{U}}{\mathrm{d}t} - \frac{\mathrm{d}\vec{\Omega}}{\mathrm{d}t} \times (\vec{r} - \vec{R}) - 2\vec{\Omega} \times \frac{\mathrm{d}(\vec{r} - \vec{R})}{\mathrm{d}t} - \vec{\Omega} \times \{\vec{\Omega} \times (\vec{r} - \vec{R})\}, \tag{2}$$

where $\vec{g}$, $\vec{U}$ and $\vec{\Omega}$ are the gravitational vector and the translational and rotational velocity vectors. In addition, $\vec{r}$ and $\vec{R}$ are the position vectors relative to o and G. The use of this internal body force is left to Eq. 4.

The sloshing-induced force acting on the ship can be obtained by integrating hydrodynamic pressures on the tank surface.
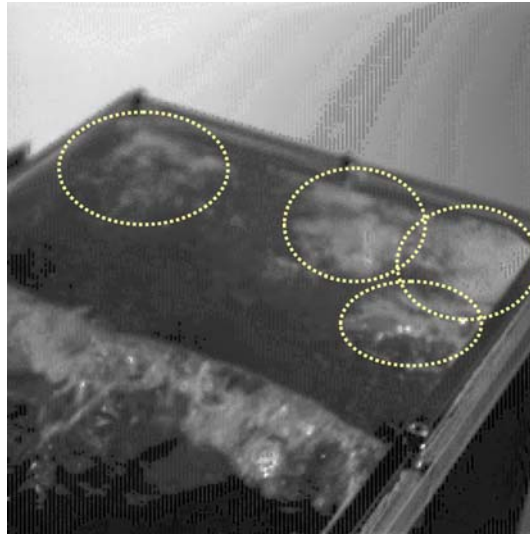
$$\vec{F}^{\text{slosh}}(t) = \int_{S_{\text{tank}}} p \left(\begin{matrix} \vec{n} \\ \vec{r} \times \vec{n} \end{matrix} \right) \mathrm{d}S, \tag{3}$$

where $\vec{n}$ indicates the normal vector of the tank surface. It should be noticed that this force includes the weight and rigid-body inertia force of fluid due to rigid-body motion, i.e., ship motion. This implies that $[m_{ij}]$ in Eq. 1 includes the fluid mass, and the ship draft for $[c_{ij}]$ reflects the fluid weight. Therefore, the quantity obtained by subtracting the hydrostatic force and rigid-body inertia force of the fluid from $\vec{F}^{\text{slosh}}(t)$ becomes $\vec{F}^{\text{internal}}(t)$.

2.2 Physical issues in sloshing problems

Sloshing flows considered in engineering applications are mostly strongly nonlinear. Violent flow phenomena, e.g. wave breaking, splashes, and impact are easily observed in sloshing flows in ship cargo. The sloshing-induced impact pressure is affected by these phenomena, making the observation and understanding of physical phenomena on these flows important for developing proper numerical models. In this paper, some physical issues observed from two experiments are described. The two experimental models introduced in this paper are the Daewoo model [17] and the SNU model. The dimensions of the tanks are 0.8 m (l: length) $\times$ 0.4 m (b: breadth) $\times$ 0.5 m (d: height) and 0.8 m(l) $\times$ 0.2 m (b) $\times$ 0.6 m (d), respectively. For the former tank, surge excitations with two amplitudes were applied, and nine strain-gauge-type

Fig. 2 Air pockets
(regions inside dotted
line) on tank top: SNU
model, 90% filling

pressure sensors were installed to measure the sloshing-induced pressure. In the case of the latter tank, the regular roll motions were excited for different amplitudes and frequencies, and motion center, but the pressure was not measured.

2.2.1 Air cushioning: formation of air pocket

It has been believed that air pockets can be formed around the corner of a tank ceiling or side wall during an impact event, and that these play a role in damping the peak impact pressures. Recently, using a high-speed camera, the formation of air pockets has been demonstrated by Colagrossi et al. [18] on a side wall, and by Rognebakke and Faltinsen [19] at the corner of a tank top. They showed that the air pocket induces oscillatory impulsive pressures. According to the our experience, when a tank is highly filled, the location of an air pocket is not only the corner of the tank top but also at any position of the tank top. When the filling ratio is not very high, air pockets have been observed mostly at the top corner. However, in the case of very high filling, air pockets can be formed even in the middle of the tank ceiling.

Figure 2 is a snapshot of sloshing flow in the SNU model at 90% filling, showing a few air pockets (white-colored regions) scattered on the tank ceiling. Furthermore, it is found that the pockets can move with the fluid motion on the tank ceiling. Although some studies, e.g. [20], on the effects of air pockets during hydrodynamic impact are available, it is extremely hard to predict the formation and effects of air pockets in the ship-sloshing problem.

2.2.2 Gas-bubble formation

Gas bubbles can be observed easily in violent sloshing flows. The bubbles are formed due to feeding gas into fluid during violent free-surface motions, e.g. impact and wave breaking. According to our experimental observation, a lot of bubbles are generated after an impact occurrence. A cluster of bubbles plays a role in reducing the fluid density, which is why the impact pressure must be damped. However, a systematic investigation of the physical phenomena and their effects is very difficult, and such studies are rare. Therefore, the effects of bubbles are one of the future issues for a more accurate prediction of sloshing-induced impact pressure.

Figure 3 shows two different cases of air-bubble formation. Figure 3a is a snapshot just before an impact occurrence on the side wall. A pack of bubbles with a small air pocket is formed near a breaking wave.
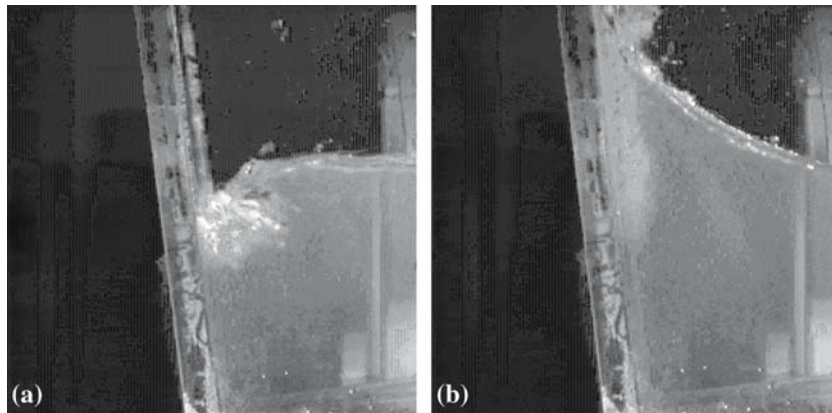
Fig. 3 Formation of bubbles before and after side-wall impact: SNU model, 30% filling. (**a**) Before impact (**b**) After impact and wave run-up

Fig. 4 Formation of bubbles during tank-top impact: Daewoo model, 80% filling
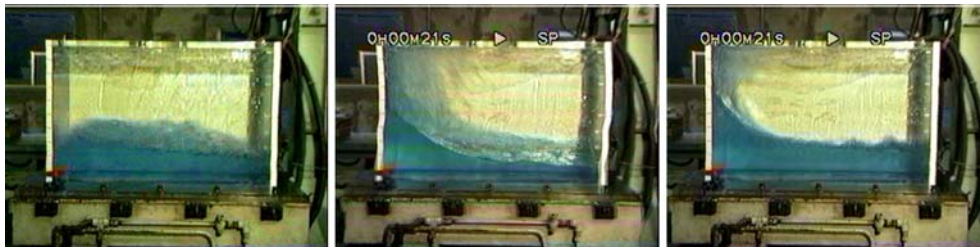

Fig. 5 Splashes after side-impact occurrence: Daewoo model, 30% filling

These bubbles are scatted along the tank wall after impact, as shown in Fig. 3b. Figure 4 shows a bigger cluster of bubbles during impact on a tank top. In the case of high filling, there are more chances to create gas bubbles due to the wide range and longer duration of impact.

2.2.3 Wave breaking and splashes

Wave breaking and splashes are typical phenomena observed in violent sloshing flows. Figure 5 shows three snapshots of sloshing flow at low filling. In general, the nonlinearity of sloshing flow becomes dominant for lower-filling situations. For instance, at shallow depth, the formation of an hydraulic jump or wave breaking is frequent. A typical process of impact under low-filling conditions is (i) formation of strongly nonlinear free-surface flow, (ii) impact on side wall, and (iii) wave run-up along the wall and splash generation. On
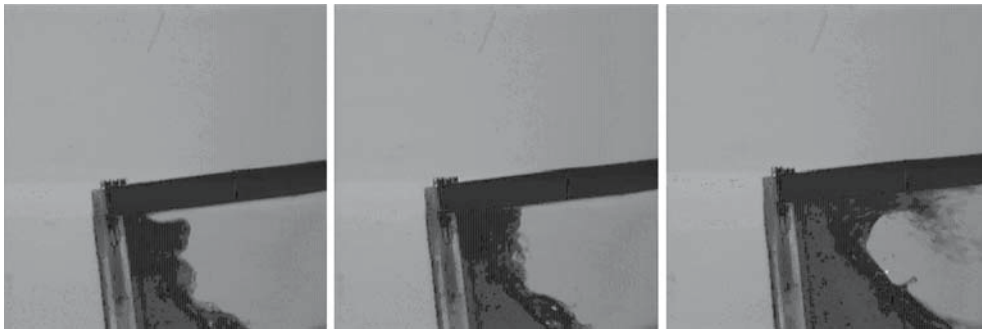
Fig. 6 Occurrence of tank-top impact and formation of splashes: SNU model, 50% filling
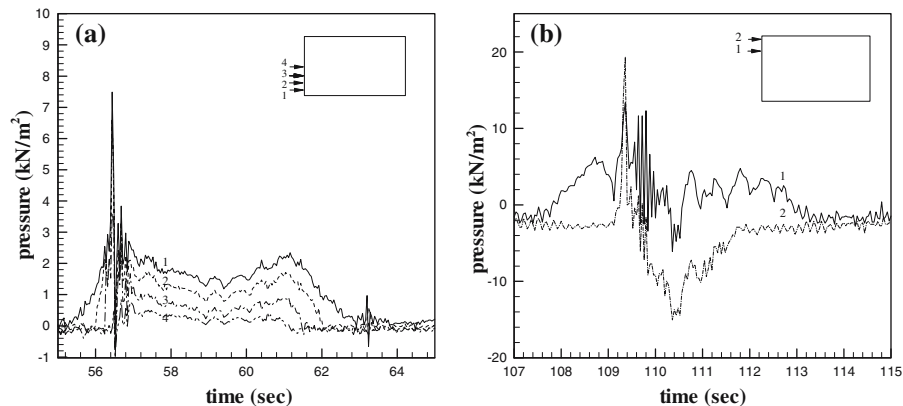

Fig. 7 Pressure signals at multiple locations: Daewoo model. (**a**) 30% filling (**b**) 70% filling

the other hand, wave breaking in high filling does not occur frequently, but a lot of splashes are formed after tank-top impact, as shown in Fig. 6.

It is doubtful that splashes provide a significant contribution to impact or global fluid motion. Our experimental observation shows that splashes are generated after impact occurrence, as shown in Figs. 5 and 6. Furthermore, local wave breaking is not likely to affect the global motion of sloshing flow. This means that local splashes and wave breaking may be ignored when the global fluid motion is concerned.

2.2.4 Hydroelasticity

Figure 7 shows two examples of an unconventional pressure time-history measured at multiple locations along tank walls at the same time. After impact occurrences on the side wall (Fig. 7a) and tank top (Fig. 7b), the pressure signals show high-frequency oscillations. This seems due to the hydroelasticity of tank structures. In fact, there is another possibility that air pockets generate oscillatory signals. However, oscillatory pressure due to the oscillation of air pockets is more local. In the two cases of Fig. 7, the oscillations of signals are more global, so that all the sensors provided high-frequency signals. In the particular case of Fig. 7b, the pressure measured at the side wall (location 1) shows a larger oscillatory signal than that at the tank corner (location 2). Considering the timing and magnitude of the oscillation, this is an obvious evidence of the vibration of the side-wall plat after the impact on the tank ceiling.

To observe the effects of hydroelasticity, we need to carry out the structural analysis coupled with sloshing flow. So far the study on this issue is very limited due to technical difficulties. It is expected that some

important information can be obtained by the numerical analysis of the coupled problem, but a proper spatial and temporal modeling of the pressure signal is necessary for such an analysis.

3 Numerical methods

In the present study, two numerical methods are applied for the simulation of sloshing flows: a finite-difference method (FDM) and a SPH method. The problem coupled with ship motion is also considered.

3.1 Finite-difference method

In this method, the details of the local flow are not of primary concern. As described above, it is assumed that the global fluid motion plays the most important role in the sloshing-induced impact occurrence. Kim [6] and Lee et al. [17] carried out a successful computation using the SOLA scheme proposed by Hirt et al. [21] for three-dimensional tanks with and without sloping boundaries, and the present study applies the same numerical scheme.

   The incompressible Euler equation and continuity equation are the governing equations of the present method. To solve these equations, let us consider the discretization of the tank volume into finite meshes. Adopting the concept of the Cartesian staggered grid, we define the velocity components on the cell boundaries, while the pressure is computed at the center of each cell. In the SOLA scheme, an iterative method is applied to the computation of instantaneous pressure and velocities. The first step of the iteration is to compute the pseudo velocity such that

$$\vec{u}^*_{ijk} = \vec{u}^{(n)}_{ijk} + \Delta t \left[-\frac{1}{\rho}(\hat{\nabla}p)^{(n)}_{ijk} + (\vec{f})^{(n+1)}_{ijk} \right] - \Delta t \{\vec{u} \cdot \hat{\nabla}\}^{(n)}_{ijk} \vec{u}^{(n)}_{ijk}, \tag{4}$$

where Δt is the temporal segment, and $\hat{\nabla}$ indicates the discrete gradient. The subscript, ijk, indicates the cell index for the x-,y-, and z-directions and the superscript (n) denotes the nth time step. Substituting (4) in the continuity equation, we can compute the pressure correction Δp_{ijk} as follows:

$$\Delta p_{ijk} = -\frac{\rho(\hat{\nabla} \cdot \vec{u}^*_{ijk})}{2\Delta t \left(1/\Delta x^2_i + 1/\Delta y^2_j + 1/\Delta z^2_k \right)}, \tag{5}$$

where $\Delta(x, y, z)$ are the spatial segments. Then, the actual velocity can be written as

$$\vec{u}^{(n+1)}_{ijk} = \vec{u}^*_{ijk} + \Delta p_{ijk} \frac{\Delta t}{\rho\{\Delta x_i, \Delta y_j, \Delta z_k\}}. \tag{6}$$

Correction of pressure and velocity, using Eqs. 5 and 6, should be carried out for all the cells in the fluid domain. Again, the corrected velocity can then be substituted in Eq. 5 for another pressure correction, and this iteration can be continued until the pressure correction is obtained within a specified error criterion.

   The solution is sensitive to the finite-difference formulation for the convection term. In the present computation, a combination of the 2nd-order central difference and the 1st-order upwind difference is applied.

   In this method, the strong assumption of a single-valued free-surface profile is applied. As mentioned above, the present method aims to simulate global fluid motion. Then this assumption provides very reasonable results, especially in high-filling conditions, as shown by Kim [6]. When this is the case, the discrete form of the kinematic free-surface boundary condition takes the following form:

$$\eta^{(n+1)}_{ij} = \eta^{(n)}_{ij} + \Delta t \left\{ w^{(n+1)}_{\eta} - u^{(n+1)}_{\eta} \left(\frac{\partial \eta}{\partial x} \right)^{(n)}_{ij} - v^{(n+1)}_{\eta} \left(\frac{\partial \eta}{\partial y} \right)^{(n)}_{ij} \right\}, \tag{7}$$

where η_{ij} indicates the wave elevation at the (i, j) column. Further, w_η, u_η, v_η are the velocity components on the free surface, which can be obtained by interpolation. In particular, a numerical filtering can be applied to avoid the instability due to saw-tooth waves.

The dynamic pressure condition can be satisfied at the cells where the free surface intersects by using a three-dimensional irregular-star method. This method is based on the Taylor-series expansion of the pressures at six neighboring points. At a cell where the free surface intersects, the pressure at the center is written as follows:

$$p_0 = c_0 \left(\frac{l_2 p_1 + l_1 p_2}{c_1} + \frac{l_3 p_4 + l_4 p_3}{c_2} + \frac{l_5 p_6 + l_6 p_5}{c_3} \right), \tag{8}$$

where

$$c_0 = \frac{l_1 l_2 l_3 l_4 l_5 l_6}{l_1 l_2 l_3 l_4 + l_3 l_4 l_5 l_6 + l_5 l_6 l_1 l_2}, \quad c_1 = l_1 l_2 (l_1 + l_2), \quad c_2 = l_3 l_4 (l_3 + l_4), \quad c_3 = l_5 l_6 (l_5 + l_6) \tag{9}$$

and l_i is the distance to the ith neighbor point. If the ith neighbor point is located on the free surface, p_i should be equal to p_{atm}. For the single-valued free-surface profile, it is possible to impose p_{atm} at a maximum of five points.

An additional no-shear condition is necessary on the free surface, which can be imposed on the velocity components in the free-surface cells. In other words, at the cells where the free surface intersects, the velocity components outside the fluid domain are controlled to have zero-shear stress. Also the free-slip condition has been applied on the tank boundaries. Furthermore, all internal members are considered to be solid plates with zero thickness.

3.2 Smoothed-particle-hydrodynamics (SPH) method

In the SPH method, a certain physical quantity $f(\mathbf{x})$ in a fluid domain Ω and its derivatives are approximated using a particle concept, taking the following forms:

$$f(\mathbf{x}) = \int_\Omega f(\mathbf{y}) \delta(\mathbf{x} - \mathbf{y}) \mathrm{d}V \approx \int_\Omega f(\mathbf{y}) W(\mathbf{x} - \mathbf{y}; h) \mathrm{d}V \approx \sum_j f(x_j) W(x - x_j; h) \frac{m_j}{\rho_j}, \tag{10}$$

$$\nabla f(\mathbf{x}) = \int_\Omega f(\mathbf{y}) \nabla \delta(\mathbf{x} - \mathbf{y}) \mathrm{d}V \approx \int_\Omega f(\mathbf{y}) \nabla W(\mathbf{x} - \mathbf{y}; h) \mathrm{d}V \approx \sum_j f(x_j) \nabla W(x - x_j; h) \frac{m_j}{\rho_j}, \tag{11}$$

where $\delta(\mathbf{x} - \mathbf{y})$, $W(\mathbf{x} - \mathbf{y}; h)$ are the delta function and a kernel function as a kind of numerical delta function. In addition, m_j and ρ_j are the mass and density of the jth particle, respectively. Under the assumption of inviscid and weakly incompressible fluid, sloshing flow is governed by the Euler equation and the continuity equation, which are expressed in the SPH approximation as

$$\frac{\mathrm{d}\rho_i}{\mathrm{d}t} = -\rho_i \sum_j (\mathbf{u}_j - \mathbf{u}_i) \cdot \nabla W_{ij} \frac{m_j}{\rho_j}, \tag{12}$$

$$\frac{\mathrm{d}\mathbf{u}_i}{\mathrm{d}t} = -\frac{1}{\rho_i} \sum_j \left(p_j + p_i + \prod_{ij} \right) \nabla W_{ij} \frac{m_j}{\rho_j} + f_i, \tag{13}$$

$$\frac{\mathrm{d}\mathbf{x}_i}{\mathrm{d}t} = \mathbf{u}_i, \tag{14}$$

where, ρ_i, $\mathbf{u}_i$ and $\mathbf{x}_i$ are fluid density, velocity and the position of ith particle, respectively. Further, f_i is the external force described in Eq. 2.

In this method, the pressure is uniquely determined by the fluid density through the equation of state [22]

$$P(\rho) = \beta \left[\left(\frac{\rho}{\rho_0} \right)^{\gamma} - 1 \right], \tag{15}$$

where ρ_0 is the reference density, and γ is a dimensionless constant chosen as 7 for water; β is a problem-dependent parameter. In practice, β is set to make the Mach number ten or more. In general, water density is the reference density. The selection of a proper value of β is a numerical issue for which a sensitivity study is needed, and it will be introduced elsewhere.

Among many candidates of kernel functions, the Gaussian kernel with smoothing length δ is used in this study because of better stability properties and computational efficiency;

$$W(s,h) = \frac{1}{\pi \delta^2} e^{-(s/\delta)^2}, \qquad \text{where,} \quad s = |\mathbf{x} - \mathbf{y}|. \tag{16}$$

In the numerical method involving time-marching, it may be hard to enforce exactly the consistency between mass, density and occupied area. It would be possible to alleviate this problem by imposing the following equation at time steps with a certain interval [9]

$$\rho_i = \sum_j m_j W_{ij}. \tag{17}$$

The Monaghan-type artificial viscosity has been widely used so far in the SPH literature. The formulation is as follows.

$$\prod_{ij} = \begin{cases} -\alpha \mu_{ij} \dfrac{c_i + c_j}{\frac{1}{\rho_i} + \frac{1}{\rho_j}}, & (\mathbf{u}_i - \mathbf{u}_j) \cdot (\mathbf{x}_i - \mathbf{x}_j) < 0, \\ 0, & (\mathbf{u}_i - \mathbf{u}_j) \cdot (\mathbf{x}_i - \mathbf{x}_j) \geq 0, \end{cases} \tag{18}$$

where

$$\mu_{ij} = \delta \frac{(\mathbf{u}_i - \mathbf{u}_j) \cdot (\mathbf{x}_i - \mathbf{x}_j)}{\left| \mathbf{x}_i - \mathbf{x}_j \right|^2 + \eta^2}. \tag{19}$$

In these expressions, c is the speed of sound determined from the state equation, and the factor η is a small number introduced to prevent numerical divergence. This expression is linear in the velocity differences, which produces a shear and bulk viscosity. It prevents unphysical penetration of particles approaching each other. In the calculations, we take $\alpha = 0.01$ and $\eta = 0.1\delta$.

A free-slip condition is imposed on solid-wall boundaries. There are a few different methods to treat the boundary particles. In this paper, the condition is satisfied by distributing "ghost particles" with density, pressure and velocity deduced from those of the physical particles adjacent to the solid boundary. The characteristics given to the ghost particles of the ith particle are:

$$\begin{aligned} p_{\text{ghost}} &= p_i, \quad \mathbf{x}_{\text{ghost}} = 2\mathbf{x}_{\text{wall}} - \mathbf{x}_i, \\ \mathbf{u}_{\text{ghost}} \cdot \mathbf{n} &= 2\mathbf{U}_{\text{wall}} \cdot \mathbf{n} - \mathbf{u}_i \cdot \mathbf{n}, \quad \mathbf{u}_{\text{ghost}} \cdot \mathbf{t} = \mathbf{u}_i \cdot \mathbf{t}, \end{aligned} \tag{20}$$

where $\mathbf{n}$ and $\mathbf{t}$ are, respectively, the normal and tangential vector on the solid wall.

The fourth-order Adams–Bashforth–Moulton scheme is used for time-marching. This time step should be chosen small enough to fulfill the following Courant–Friedrichs–Levy (CFL) type:

$$\Delta t = \beta \min_j \left(\frac{h}{c_i + \sigma_i} \right), \quad \sigma_i = \max \left| h \frac{(\mathbf{u}_j - \mathbf{u}_i) \cdot (\mathbf{x}_j - \mathbf{x}_i)}{\left| \mathbf{x}_j - \mathbf{x}_i \right|^2} \right|. \tag{21}$$

A well-known problem of the SPH method is the accuracy of the pressure. In the present computation, three different approaches are considered: (i) conventional interpolation from neighbor particles, (ii) correcting hydrostatic component, and (iii) pressure-sensor concept [11]. All the methods provide spiky behavior of the pressure signal. Therefore, we observe only the sloshing-induced force in the present SPH computation.

3.3 IRF method for ship motion

When the concept of impulse-response function is invoked for the radiation force, the equation of motion, (1), can be rewritten to the following form:

$$\sum_{j=1}^{6} \left[(m_{ij} + a_{ij}(\infty))\ddot{\xi}_j(t) + \int_0^t R_{ij}(t-\tau)\dot{\xi}_j(\tau)\mathrm{d}\tau + c_{ij}\xi_j(t) \right] = F_i^{\mathrm{ext}}(t) + F_i^{\mathrm{slosh}}(t), \tag{22}$$

where $a_{ij}(\infty)$ represents the infinite-frequency added mass. Here $R_{ij}(t)$ is the so-called retardation function. $F_i^{\mathrm{ext}}(t)$ is the wave-excitation force acting externally on the hull, while $F_i^{\mathrm{slosh}}(t)$ is the sloshing-induced force acting internally on the tank.

The retardation function corresponds physically to the response of a body to a unit impulsive velocity. Fundamental properties of the retardation function for the radiation force are that these functions are real, and, from the principle of causality, they must vanish for $t < 0$. The formulas for $a_{ij}(\infty)$ and $R_{ij}(t)$ are given by

$$R_{ij}(t) = \frac{2}{\pi} \int_0^\infty b_{ij}(\omega)\cos(\omega t)\mathrm{d}\omega = -\frac{2}{\pi} \int_0^\infty \omega\{a_{ij}(\omega) - a_{ij}(\infty)\}\sin(\omega t)\mathrm{d}\omega, \tag{23}$$

$$a_{ij}(\infty) = a_{ij}(\omega) + \frac{1}{\omega} \int_0^\infty R_{ij}(t)\sin(\omega t)\mathrm{d}t, \tag{24}$$

where $a_{ij}(\omega)$ and $b_{ij}(\omega)$ are the added-mass and damping coefficients, respectively. Therefore, the retardation function can be computed using either a damping coefficient or an added mass. From computational experience, a significant difference is not found. In the present computation, the damping coefficients are used to obtain the retardation function.

In an actual numerical computation of the retardation function, a truncation error is inevitable since the integral of Eq. 23 is generally carried out in a finite frequency range. To minimize this truncation error, a special treatment similar to that of Lee and Newman [23] is applied. Let us consider the inverse transform of the retardation function as follows:

$$b(\omega) = \int_0^\infty R_{ij}(t)\cos(\omega t)\mathrm{d}t = \left[R_{ij}(t)\frac{\sin(\omega t)}{\omega} \right]_0^\infty + \left[R_{ij}'(t)\frac{\cos(\omega t)}{\omega^2} \right]_0^\infty - \int_0^\infty R_{ij}''(t)\frac{\cos(\omega t)}{\omega^2}\mathrm{d}t$$

$$= -R_{ij}'(0)\frac{1}{\omega^2} + O(\omega^{-3}). \tag{25}$$

For a sufficiently large Ω, the retardation function with a correction of the truncation error can be approximated using (25):

$$R_{ij}(t) = \frac{2}{\pi} \int_0^\Omega b_{ij}(\omega)\cos(\omega t)\mathrm{d}\omega + \varepsilon_{ij}(t), \tag{26}$$

where

$$\varepsilon_{ij}(t) \equiv \frac{2}{\pi} \int_\Omega^\infty b_{ij}(\omega)\cos(\omega t)\mathrm{d}\omega \simeq -\frac{2}{\pi}R_{ij}'(0) \int_\Omega^\infty \frac{\cos(\omega t)}{\omega^2}\mathrm{d}\omega = -\frac{2}{\pi}R_{ij}'(0)\frac{\cos(\Omega t) + \Omega t\,\mathrm{si}(\Omega t)}{\Omega} \tag{27}$$

and $\mathrm{si}(z)$ is the sine integral.

The constant $R_{ij}'(0)$ can be calculated by numerical difference if the time step is sufficiently small.

To include viscous roll damping, we define an equivalent linear damping coefficient as follows:

$$b_{44} = 2\gamma\sqrt{\{m_{44} + a_{44}(\infty)\}c_{44}}, \tag{28}$$

where γ is a constant and $2\sqrt{\{m_{44} + a_{44}(\infty)\}c_{44}}$ is the critical damping coefficient of the roll motion. Therefore, γ indicates a ratio to the critical roll damping. For typical ships, γ is in the range of 0.02 and 0.05.

For surge, sway, and yaw motions, the concept of soft spring is adopted to prevent monotonically increasing or decreasing motion. The soft spring can be considered as a mooring system or an autopilot. The strength of the soft spring is related to the period of oscillatory motion due to the spring, and this period should be much longer than that of the wave-excitation period.

3.4 Technical issues

The physical issues described above should be considered in the numerical methods for a realistic simulation of sloshing flows. To achieve this, several technical issues are introduced here.

3.4.1 Sensitivity to computational parameters

Since the numerical computation is carried out in a discrete spatial (cells or particles) and time domain, the sensitivity to the discretization parameters should be carefully observed. In the case of FDM, Lee et al. [17] carried out a systematic observation of the sensitivity of the impact pressure to mesh size, time segment, averaging time interval, and the size of the buffer zone. In particular, they observed that the application of pressure-averaging and buffer zone mitigates the sensitivity. The parameters which should be considered in the SPH method are somewhat different from those of FDM. A systematic investigation for the SPH method is in progress, and some results are introduced in the computational results of the present paper.

3.4.2 Simulation of global and local flows

The sloshing flow we are interested in here is strongly nonlinear. That is, the sloshing flow to be solved is very violent in most cases. From a viewpoint of computational effort, an accurate prediction of such a flow is an extremely hard. As mentioned above, when the primary concern is an accurate prediction of the slosh-induced impact pressure and/or force, it is reasonable to assume that local flows do not play a significant role in the impact occurrence. According to our observation of the experimental data, over-turning waves and splashes occur after the primary impact. This indicates that the magnitude of the impact pressure may depend on the global motion of sloshing flows, not on wave-overturning or splash. Therefore, the simulation of such global flows is a key factor in predicting slosh-induced impact. This is not exactly true as the filling depth becomes shallower. In shallow-depth flow, hydrodynamic impact on a side wall occurs when a hydraulic jump is formed and hits the wall. However, even in such a case, the resultant impact is still significantly dependent on global fluid motion.

3.4.3 Discontinuous impact signal

Since we solve the problem in a discrete domain, the time-history of the impact pressure may show a spiky behavior. To mitigate such spiky behavior, time-averaging can be used. This method has been introduced by LLOYD Register of shipping and also by Kim [6]. This method makes spiky impact signals more continuous by taking the following form:

$$p_{\text{avg}}(\bar{t}^{(n)}) = \frac{1}{N} \sum_{n=1}^{N} p(t^{(n)}),$$
(29)

where

$$\bar{t}^{(n)} = \frac{1}{N} \sum_{n=1}^{N} t^{(n)}.$$
(30)

As shown by Lee et al. [17], this scheme provides some benefits in the analysis of impact pressure. According to numerical experience, $N = 3$ or 4 provides a reasonable magnitude of the impact peak.
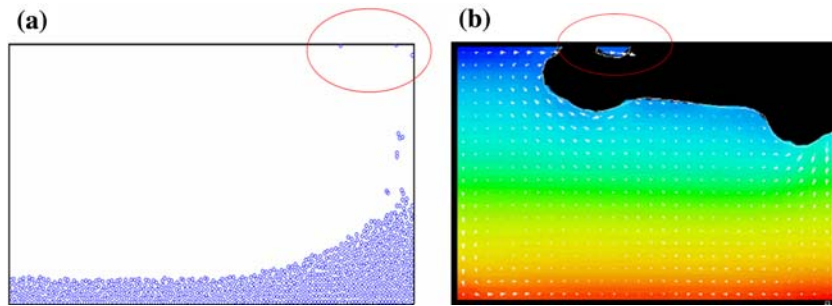
Fig. 8 Attachment of fluid volume on tank ceiling. (**a**) SPH Method (**b**) FLOW3D

3.4.4 Boundary conditions on tank ceiling: proper detachment

Two types of wall boundary condition can be considered in numerical computations; no-slip and free-slip conditions. Either condition should be combined with a no-flux condition which prescribes that no water particle penetrates the tank wall. It is found that the no-flux condition can result in unrealistic flow, especially on the tank ceiling. Theoretically speaking, nothing is wrong with this condition. However, due to the coarse resolution of the numerical method, the no-flux condition tends to make fluid stay on the tank boundary. For instance, Fig. 8 shows two snapshots of computational results obtained by the conventional SPH method and a general-purpose commercial program. In these figures, fluid volumes are not detached properly from the tank ceiling. In a gravity field, these are non-physical. To cure this problem, the realistic attachment and detachment should be properly implemented in a numerical computation.

3.4.5 Buffer zone: impact simulation in FDM

The magnitude of the impact pressure can be sensitive to local physical phenomena such as air cushioning, bubble formation, and hydroelasticity. Unfortunately, these local phenomena are very complicated to analyze. Moreover, considering all these effects in the prediction of impact pressure is extremely difficult.

As a remedy for the unphysical sensitivity of impact pressure to time segment and also for including the effects of local phenomena, Kim [6] applied a mixed condition of the free-surface and wall conditions within a certain region beneath the tank ceiling, the so-called buffer zone. In the buffer zone, the boundary condition on free surface takes the following form:

$$F = \kappa \frac{p - p_{\text{atm}}}{\rho} + (1 - \kappa) \frac{H_B}{\Delta t} V_N = 0, \tag{31}$$

where κ is the weight of the free-surface boundary condition which is written as

$$\kappa = \begin{bmatrix} (\eta_{\max} - \eta)/H_B & \eta_{\max} - H_B \leq \eta < \eta_{\max} \\ 1 & \eta \leq \eta_{\max} - H_B, \\ 0 & \eta = \eta_{\max} \end{bmatrix} \tag{32}$$

where $\eta_{\max}$ means the height of the tank ceiling and H_B is the size of the buffer zone.

In the present computation using FDM, this condition is applied during impact occurrence on tank top and hopper. In the case of the SPH method, this has not been applied yet.

3.4.6 Implicit coupling of sloshing and ship motion

The problem of sloshing and ship motion is implicitly coupled. That is, the two problems should be solved simultaneously. To achieve this implicit coupling in numerical computation, an iterative scheme seems the
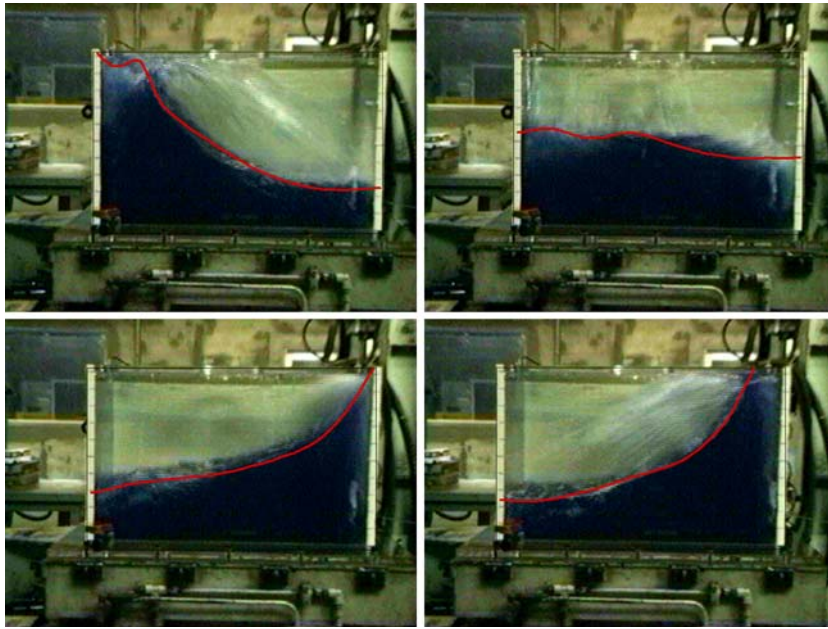
Fig. 9 Comparison of free-surface profiles with experiment: Daewoo model, FDM, 50% filling, 0.04-cm amplitude, 1.68-Hz frequency

only way since the sloshing flow is fully nonlinear. However, the iteration at each time requires a great computation effort, especially CPU time. In the present computation, it is assumed that the sloshing-induced forces and moments do not change much during the time segment for the computation of ship motion. Furthermore, the ship motion is slowly varying during the time segment of sloshing simulation. When this is the case, the coupling can be done in an explicit manner at each time step. Kim [13] showed that this approach provides reasonable results in the coupled problem. In general, the time segment for ship motion is larger than that for sloshing flow.

4 Computational results

Numerical computations have been carried out for three models: Daewoo, SNU, and MARIN models. Van Daalen et al. [24] carried out a series of experiment at MARIN to measure the sloshing-induced roll moments in a tank of dimension, 0.1 m(l) × 1.0 m(b) × 0.5 m(d). In the present computation, the FDM and SPH method are applied for these models, and the results are compared. In the coupled problem, the IRF computation of the ship motion is coupled with the FDM program.

4.1 Sloshing problem

Figure 9 shows a comparison of free-surface profiles between the experimental observation and the results of FDM. Despite ignoring splashes after impact, the agreement of global fluid motion is very fair, as expected.

Figure 10 compares the computed hydrodynamic pressure on a side wall with experimental data, showing a very nice agreement of the overall trend. In the experimental data, very sharp peaks appear from time to time, and this may be due to strong violence of sloshing flows, e.g. hydraulic jumps. To simulate such violent flows, the present FDM should be extended to treat the multi-valued free-surface profile.
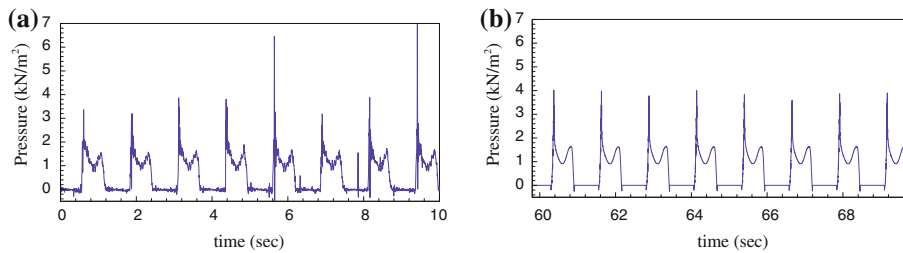
Fig. 10 Comparison of the time-histories of pressure between experiment and computation: FDM, Daewoo model, 30% filling, 4-cm and 0.79-Hz excitation. (**a**) Experiment (**b**) Computation
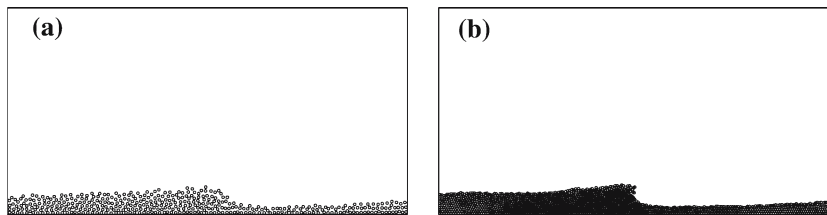

Fig. 11 Maximum pressure at the corner of the tank ceiling: FDM, Daewoo model, 50% filling. (**a**) 0.02-cm amplitude (**b**) 0.04-cm amplitude
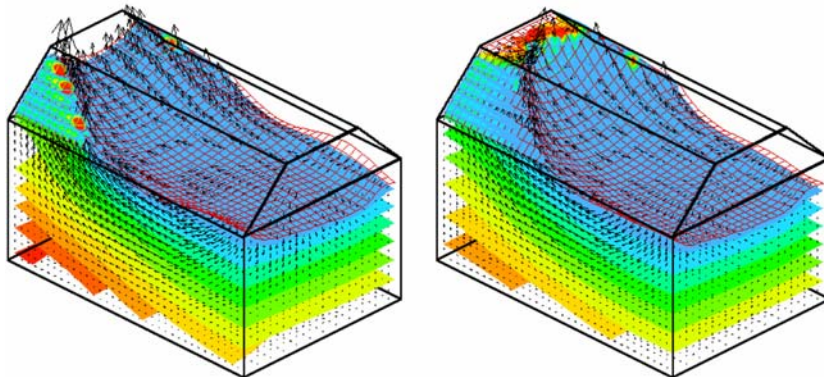

Fig. 12 Example of a computation for three-dimensional sloshing flows: from [7], $l/b = 1.5$, $h/b = 1.0$, $h/d = 0.7$, $h_u/d = b_u/b = 0.27$, $\xi_{4,0} = 10$-deg, $\omega/\sqrt{g/l} = 1.92$

A comparison of the maximum pressure at the corner of the tank ceiling is shown in Fig. 11 for the Daewoo model. These pressures are the largest quantities observed at all frequencies. As is easily understood, the value of the peak pressure is dependent on the time-averaging. Time-averaging provides a kind of smoothing effect, so the peak pressure reduces when more intervals are applied.

The present FDM method can be extended to three-dimensional problems. Figure 12 shows an example of such an extension introduced by Kim et al. [7].

In the present study, the SPH method has been applied mostly for the MARIN model to compare the roll moment with experimental data. It is found that the computed global forces and moments are not sensitive to particle number. However, local flow and local pressure can be significantly dependent on particle number. Figure 13 shows a comparison of fluid domains for different particle resolution at the same instantaneous time. A more detailed wave front is clearly shown. Furthermore, it is found that a more
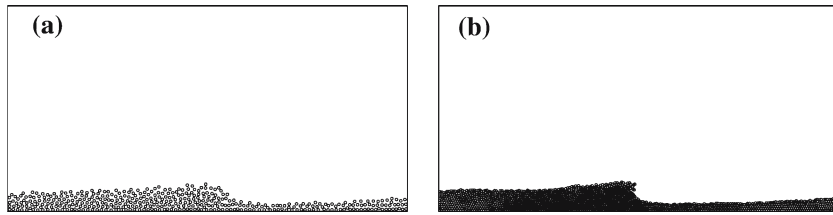
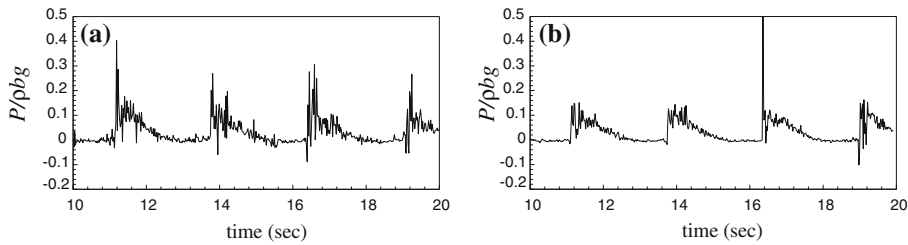**Fig. 13** The effects of particle numbers: SPH, 0.0667-rad roll amplitude, t=16.35-s. (**a**) 100×4 particles (**b**) 200×8 particles

Fig. 14 Effects of resolution on local pressure: SPH, h/b=0.04, $\omega_\phi = 3.0$ rad/sec (**a**) 100×4 particles (**b**) 200×8 particles
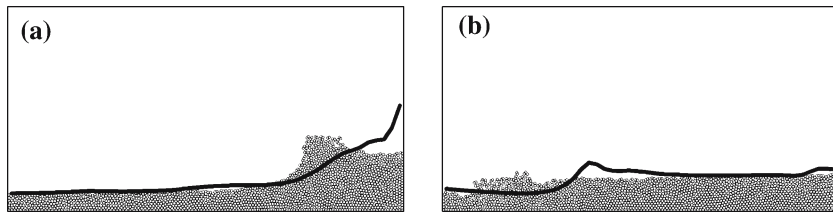

Fig. 15 Comparison of free-surface profiles between FDM and SPH: MARIN model, $\omega_\phi = 3.1, h/b = 0.08, 150 \times 12$ particles, solid line: FDM, small circle particles: SPH. (**a**) 8.1 sec (**b**) 8.6 sec

stable time-history of pressure is observed for a larger number of fluid particles. Such a trend is obvious in Fig. 14.

The SPH results are compared also with those of FDM. Figure 15 shows a comparison of the free-surface profile between the SPH and FDM results at $h/b = 0.08$ and 0.10. Two profiles show a slight phase difference, since the velocity of the bore flow in the SPH simulation is faster than that of FDM. Figure 16 compares the time-histories of the roll moment, obtained by the two numerical methods. Despite the agreement of the amplitude at the excitation frequency, the SPH provides a very spiky signal. The amplitudes of the roll moment are summarized in Fig. 17. It is obvious that the two methods agree well with experimental data. As the filling depth becomes shallower, more nonlinear wave profiles can be generated. Then, the application of the SPH method is more effective to capture such strongly nonlinear profiles, e.g. wave breaking. However, in general, the FDM computation is more stable, as shown in Fig. 16.

Figure 18 plots the measured and computed roll amplitudes and phases between experimental and computational results. In this case, the axis of rotation is fixed at the tank bottom and the oscillation amplitude is 3.8 degrees. Time marching is performed using the fourth-order Adams–Bashforth–Moulton method with a fixed time step. The amplitude and phase of the roll moment show excellent agreement, except the amplitude at $h/b = 0.1$ and the phase at $h/b = 0.04$ in the region of high frequencies. The discrepancies may be due to strong nonlinearity.

Fig. 16 Comparison of the time-histories of roll moment: FDM vs. SPH, MARIN model, $\omega_\phi =$ 2.7 rad/sec, $h/b = 0.08$, 100×8 particles
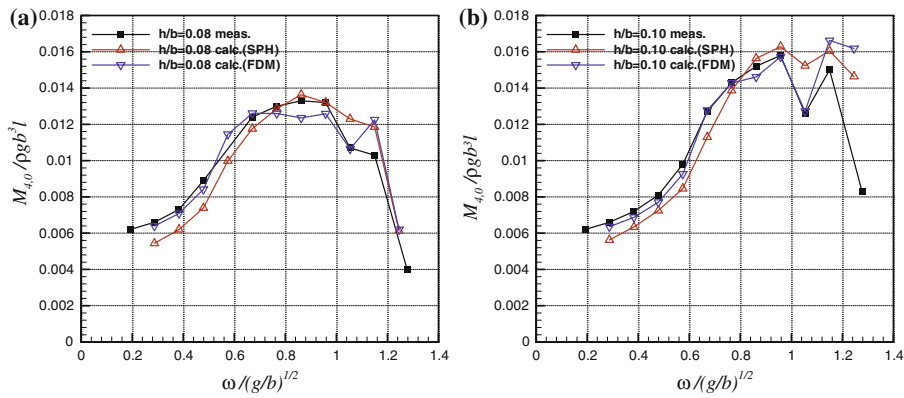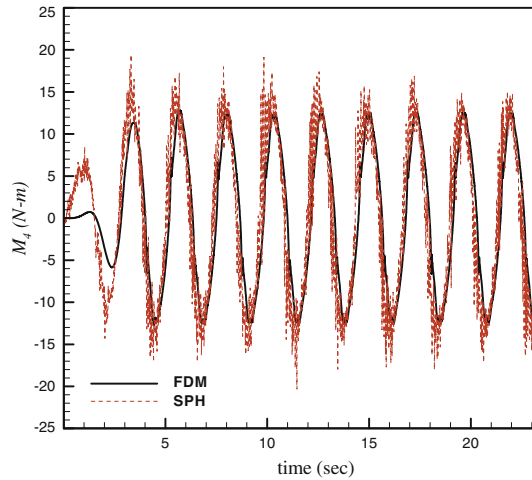

Fig. 17 Comparison of the amplitude of roll moment between the SPH and FDM results: MARIN model, roll amplitude=3.8 deg. (**a**) $h/b = 0.08$ (**b**) $h/b = 0.10$
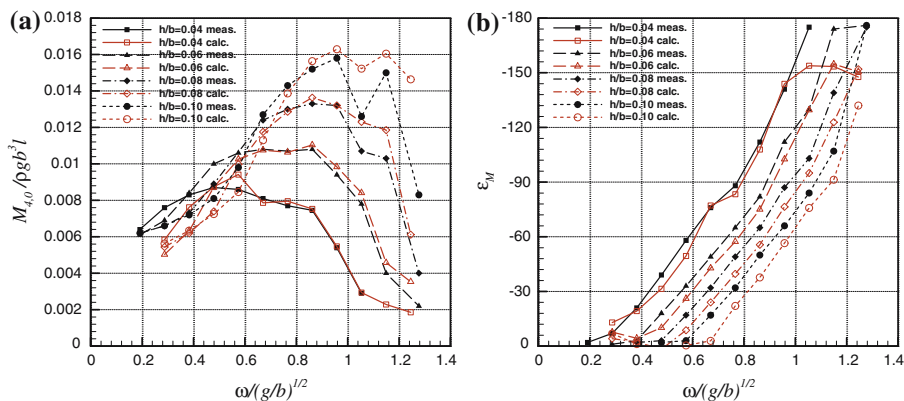

Fig. 18 Comparison of the amplitude and phase of roll moment between the SPH and experiment: MARIN model, roll amplitude=3.8 deg. (**a**) Amplitude (**b**) Phase

Fig. 19 Times-histories
of wave excitation,
sloshing-induced moment,
and the corresponding roll
motion at near-resonance
frequency: 50% filling,
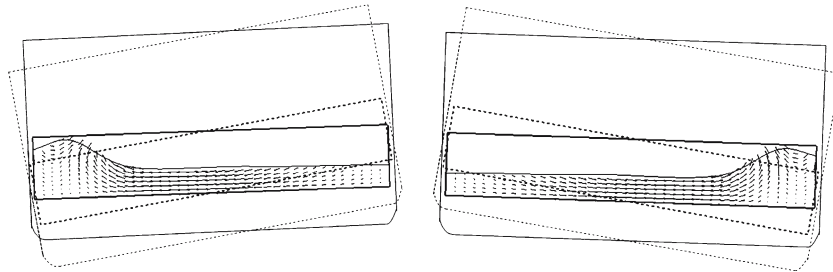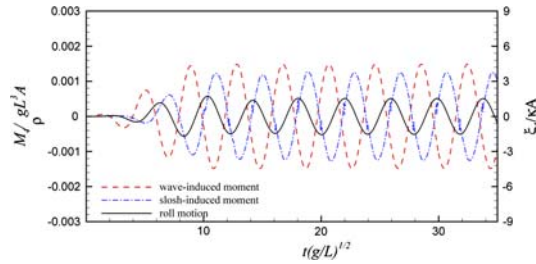$A/L = 0.01$, $\omega\sqrt{L/g} = 1.6$

Fig. 20 Comparison of ship motions with and without coupling effects: dotted line: 50% filling, $A/L = 0.01$, dotted line: without coupling, solid line: with coupling

4.2 Coupled problem

The coupled problem has been solved for the modified S175 hull introduced by Kim [13,25]. The beam (B)-length(L) and draft(D)-length(L) ratios of this hull are 0.288 and 0.084, respectively. A passive flume-type ART is equipped at $Z = 0.045L$ near midship, and its dimension normalized with respect to ship length is $0.05882(l) \times 0.2878(b) \times 0.0504(d)$. To concentrate on the roll motion, only beam sea is considered in this study. 3.0% of the critical roll damping is used for the viscous roll-damping coefficient.

In general, the roll amplitude of a ship equipped with an ART is strongly dependent on the tuning factor defined as the ratio between the natural frequencies of the roll motion and sloshing flow. When the tuning factor is close to unity, i.e., near-resonance frequency, the phase difference between the wave excitation and sloshing-induced moments is about 180 degrees, as in Fig. 19. In this case, a dramatic reduction of the roll motion can be observed due to the total moment much less than the case of wave excitation only. Figure 20 compares the instantaneous body motions with and without the ART. The reduction of roll motion is obvious, as expected.

Figure 21 plots the roll RAOs for different filling conditions and wave slopes. This result provides important information about the coupling effects, especially related to the nonlinearity of sloshing flow. In the realm of the linear theory, the roll RAOs do not change for different wave slopes. However, Fig. 21 shows the strong sensitivity of the motion RAOs to wave amplitude, A. This means that the nonlinearity of sloshing flow plays a critical role in the ship motion. This result shows also that the wave-excitation component becomes more significant in a larger wave slope. For a rectangular tank, the increment of the sloshing-induced moment becomes less as the motion amplitude becomes larger. For instance, Fig. 22 shows the sloshing-induced moment for the MARIN model as a function of roll amplitude. The roll moment increases in a nonlinear manner. On the other hand, the wave-induced moments increase linearly in the linear theory. Therefore, the motion RAOs are getting closer to those without ART as A/L becomes larger.

Figure 23 shows a comparison with the result of Kim et al. [25]. In his study, a three-dimensional panel method has been applied for the ship motion in the time domain. In particular, LAMP (Large-Amplitude Ship Motion Program) has been applied for the ship motion. The two numerical results show the same
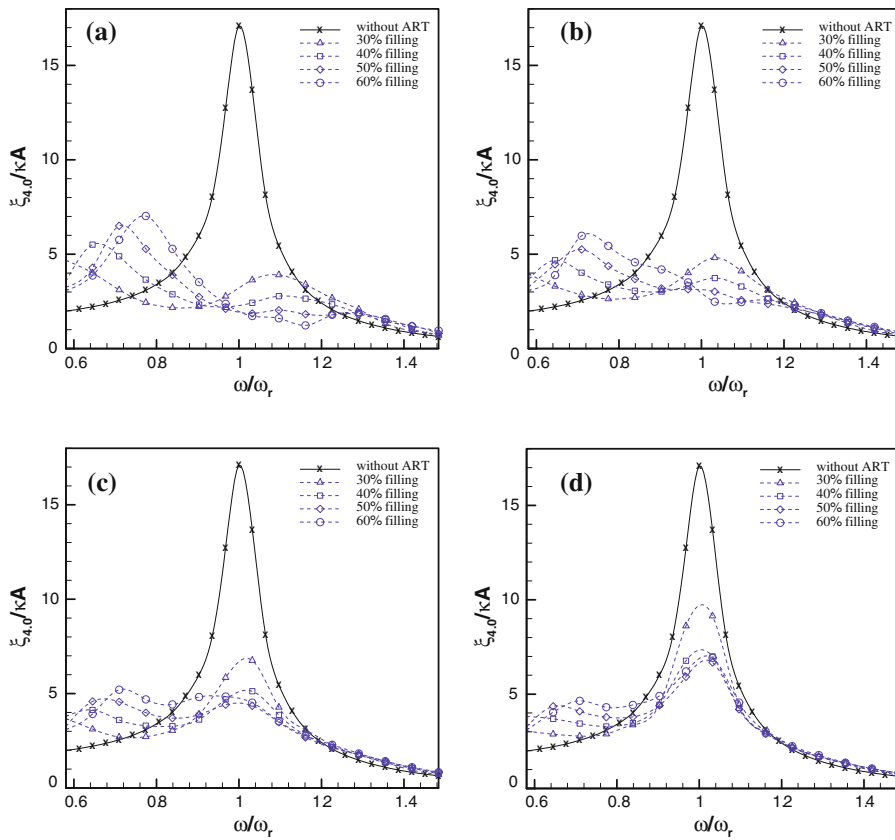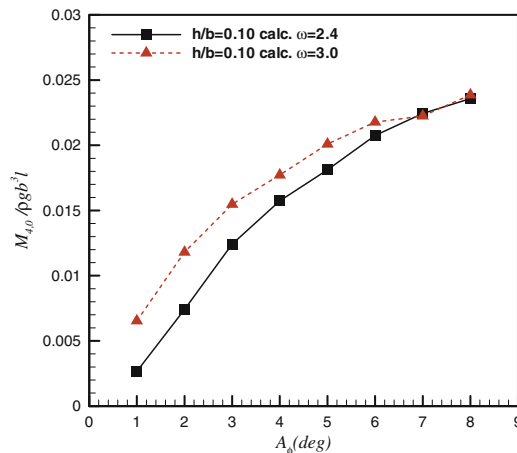
Fig. 21 Roll RAOs for different wave slope. (**a**) $A/L = 0.01$ (**b**) $A/L = 0.15$ (**c**) $A/L = 0.02$ (**d**) $A/L = 0.25$

Fig. 22 Roll moment Vs roll amplitude: MARIN model, SPH, $h/b = 0.1$

trend of motion RAOs. The difference in amplitude and peak frequency is probably due to the different computational programs. Although the same problem is solved, the LAMP program adopts the time-domain approach based on the fundamental source-distribution method, while the IRF method adopts the frequency-domain approach. Furthermore, a set of the frequency-domain solution applied for the IRF method in the present computation is obtained by the wave-Green-function method. Therefore, the use of
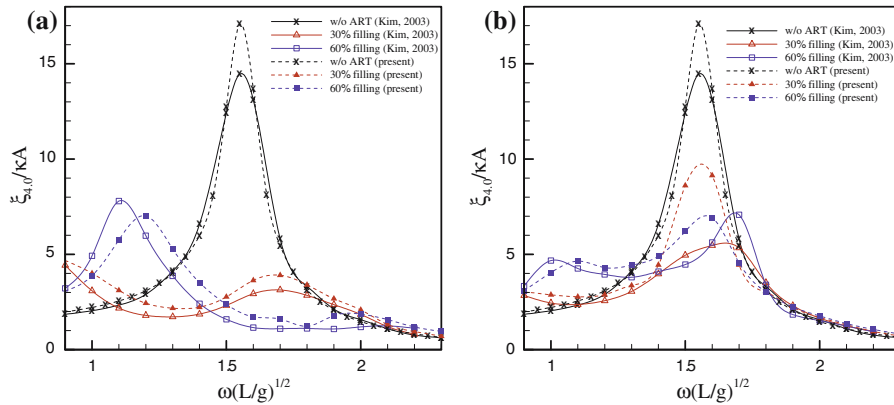
Fig. 23 Comparison with existing results [13]. (**a**) $A/L = 0.01$ (**b**) $A/L = 0.025$

different methods and the method of solution seems the primary source of the discrepancy. In the case of computational times, the present method is much more efficient than the time-domain method adopting the panel method.

5 Conclusions

In the present study, the physical and technical issues of sloshing flows in ship cargo are described. The physical phenomena in violent sloshing flows have been carefully observed in experiments, and proper numerical models are proposed. Two numerical methods, namely FDM and SPH methods, are applied to solve violent sloshing flows in the Daewoo, SNU, and MARIN models. Based on the present study, the following conclusions can be made:

– There are several physical issues which should be considered in a sloshing analysis. These issues include the effects of gas bubble, cushioning due to air pocket, local wave breaking, splashes, and hydroelasticity. To understand their effects is critical for the development of numerical models for sloshing analysis.
– There are several technical issues in the numerical simulation of violent sloshing flows. Due to discrete spatial and time domains, proper numerical techniques are essential to make the solution more continuous, stable, and realistic. Also, proper numerical treatment is critical to simulate the sloshing-induced impact occurrence.
– The concepts of buffer zone and time-averaging are helpful to mitigate the sensitivity of computational parameters. In particular, the application of a buffer zone seems useful in the prediction of impact pressure.
– The SPH method provides a less stable solution than FDM. The weakest point is in the computation of pressure, but it is applicable to predict the global sloshing-induced force and moment. To this end, a careful and systematic observation of the computational parameters is essential.
– The nonlinearity of sloshing flows plays a critical role in ship motion coupled with sloshing. The sloshing-induced force and moment are not linearly proportional to excitation amplitude. Therefore, the ship motion coupled with sloshing does not vary in a linear manner with respect to wave amplitude.
– The coupled problem is described well by a linear theory based on the impulsive response function. This method is accurate and robust, and particularly very efficient regarding computational time.

References

1. Faltinsen OM (1978) A numerical non-linear method of sloshing in tanks with two-dimensional flow. J Ship Res 18:224–241
2. Faltinsen OM, Rognebakke OF (2000) Sloshing, Int Conf on Ship and Shipping Research, NAV, Venice, Italy
3. Bridges TJ (1982) A numerical simulation of large amplitude sloshing, Proc. of the 3rd Int. Numerical Ship Hydrodynamics, Paris, France
4. Mikelis NE (1984) Sloshing in partially filled liquid tanks and its effect on ship motions: numerical simulations and experimental verification. RINA Spring meeting, London
5. Wu GX, Ma QW, Eatock-Taylor R (1998) Numerical simulation of sloshing waves in a 3D tank based on a finite element method. Appl Ocean Res 20:337–355
6. Kim Y (2001) Numerical simulation of sloshing flows with impact load. Appl Ocean Res 23:53–62
7. Kim Y, Shin YS, Lee KH (2004) Numerical study on slosh-induced impact pressures on three-dimensional prismatic tanks. Appl Ocean Res 26:213–226
8. Monaghan JJ (1994) Simulating free surface flows with SPH. J Comp Phys 110:399–406
9. Colagrossi A, Landrini M (2003) Numerical simulation of interfacial flows by smoothed particle hydrodynamics. J Comp Phys 191:448–475
10. Iglesias AS, Rojas LP, Rodriguez RZ (2004) Simulation of anti-roll tanks and sloshing type problems with smoothed particle hydrodynamics. Ocean Eng 31:1169–1192
11. Oger G, Doring M, Alessandrini B, Ferrant P (2006) Two-dimensional SPH simulations of wedge water entries. J Comp Phys 213:803–822
12. Dillingham J (1981) Motion studies of a vessel with water on deck. Marine Technol 18:38–50
13. Kim Y (2002) A numerical study on sloshing flows coupled with ship motion-the anti-rolling tank problem. J Ship Res 46:52–62
14. Rognebakke OF, Faltinsen OM (2003) Coupling of sloshing and ship motions. J Ship Res 47:208–221
15. Newman JN (2005) Wave effects on vessels with internal tanks. Proc. 20th workshop on water waves and floating bodies, Spitsbergen, Norway
16. Cummins WE (1962) The impulse response function and ship motions. *Symposium on Ship Theory*, Hamburg, Germany, Schiffstechnik 9:101–109
17. Lee YB, Kim Y, Kim YS, Shin YS (2004) Parametric study on slosh-induced impact pressures: experiment vs. numerical computation. Proc. 19th workshop on water waves and floating bodies, Cortona, Italy
18. Colagrossi A, Lugni C, Greco M, Faltinsen OM (2004) Experimental and numerical investigation of 2D sloshing with slamming, 19th workshop on water waves and floating bodies, Cortona, Italy
19. Rognebakke OF, Faltinsen OM (2003) Coupling of sloshing and ship motions. J Ship Res 47:208–221
20. Peregrine DH (2003) Water-wave impact on walls. Ann Rev Fluid Mech 35:23–43
21. Hirt CW, Nicholas BD, Romero NC (1975) SOLA-a numerical solution algorithm for transient fluid flows. Los Alamos Scientific Laboratory, Report LA-5852
22. Bachelor GK (1967) An introduction to fluid dynamics. Cambridge University Press, Cambridge
23. Lee CH, Newman JN (2005) Computation of wave effects using the panel method. Numerical models in fluid-structure interaction. WIT Press, pp 211–251
24. van Daalen EFG, van Doeveren AG, Driessen PCM, Visser C (1999) Two-dimensional free surface anti-roll tank simulations with a volume of fluid based Navier-Stokes solver. Report No. 15306–1-OE, MARIN
25. Kim Y, Shin YS, Lin WM, Yue DKP (2003) Study on sloshing problem coupled with ship motion in waves. Proc. 8th international conference on numerical ship hydrodynamics, Busan, Korea